metals

MDPI

Article

Effect of Aging Treatment on Microstructure and Properties of the $Fe_{55}(CoCrNi)_{10}(MoV)_5C_5$ Medium-Entropy Alloy

Da Hong [1], Hebin Wang [1,*], Longgang Hou [2], Ping Ou [1], Yiqi Wang [1] and Hongjin Zhao [1,*]

[1] School of Materials Science and Engineering, Jiangxi University of Science and Technology, Ganzhou 341000, China; 6720180464@mail.jxust.edu.cn (D.H.); ouping@jxust.edu.cn (P.O.); 6720180149@mail.jxust.edu.cn (Y.W.)

[2] State Key Laboratory for Advanced Metals and Materials, University of Science and Technology Beijing, Beijing 100083, China; lghou@skl.ustb.edu.cn

* Correspondence: wanghebin@jxust.edu.cn (H.W.); zhaohongjin@jxust.edu.cn (H.Z.)

Received: 30 July 2020; Accepted: 11 August 2020; Published: 13 August 2020

Abstract: In this study; the effect of aging treatment for 4 h at 600–1000 °C on the microstructure and properties of a $Fe_{55}(CoCrNi)_{10}(MoV)_5C_5$ medium-entropy alloy (MEA) was investigated. After the alloy was aged at 800 °C, a large number of granular and rod-shaped particles are formed throughout the face-centered cubic (FCC) matrix. The average particle diameter was measured to be approximately 46 nm, and the result of transmission electron microscopy (TEM) analysis verified that these secondary precipitates are VC carbides, which plays an important role for pinning dislocations and hindering dislocation movement. Therefore, the hardness and ultimate tensile strength of the alloy at this state increased from 253 HV, 322 MPa in cast condition to 326 HV, 626 MPa, respectively, while remaining relatively good elongation (6.2%). As the aging temperature increases, the volume fraction of the VC carbides decreased while its sizes increased; thus, the dispersion strengthening effect was reduced, resulting in the decrease in the hardness and strength.

Keywords: medium-entropy alloy; aging treatment; precipitation; microstructure; mechanical property

1. Introduction

High-entropy alloys (HEAs) are defined as alloys composed of five or more principal elements with the molar ratio of each principal element between 5% and 35% [1]. As one of the new materials that developed in recent years, HEAs have received more and more attention [1–12] due to their unique property differences from traditional alloys for which the composition is based on one or two principal elements. HEAs are mainly manifested as the following four core effects: high configuration entropy in thermodynamics, sluggish atomic diffusion in kinetics, severe lattice distortion effect in structure, and "cocktail" effect in performance [4]. Due to their unique high-entropy effect, HEAs are easy to form a simple solid solution structure rather than intermetallic compounds, thus exhibiting high strength, high hardness, good ductility, and excellent thermal stability [13–17].

FeCoCrNi is a typical HEA with a simple face-centered cubic (FCC) structure, possessing good ductility and fracture toughness at room temperature or liquid nitrogen temperature. However, its strength is only 145 MPa in the as-cast state, which is far from meeting the demand of practical applications [18]. In order to solve this issue, some strengthening methods, such as fine grain strengthening, dislocation strengthening, precipitation strengthening, and solution strengthening should be introduced into this alloy. Among them, precipitation strengthening is an effective method to improve the strength of FeCoCrNi HEA. T T shun et al. [19] have investigated the aging-hardening of the $FeCoCrNiMo_{0.85}$ HEA after aging at 700–1000 °C, and they found that the σ phase can be completely

transformed into the μ phase after 700 °C aging, giving rise to the hardness increasing from 420 to 621 HV. He et al. [20] have studied the strengthening mechanism of FCC precipitates in $CoCrFeNiNb_{0.25}$ HEA and found that FCC precipitates appeared in the matrix after annealing, resulting in doubling the strength without losing the plasticity. As interstitial atoms, carbon is widely used in the traditional structural materials such as steels and super-alloys due to its solid solution strengthening and carbide precipitation strengthening [21–24]. In some super-austenitic steel, the precipitation of carbide in the austenitic matrix can give rise to the outstanding strength at high temperatures. Ou et al. [25,26] observed that the dense nanosized MX phases were precipitated at the coherent Cu-rich phase with a nanosized diameter in the austenitic matrix, contributing an excellent precipitation strengthening effect and creep resistance in the Super304H austenitic steel. Anburaj et al. [27] investigated the precipitation behavior in an aged super-austenitic stainless steel and found that chi, carbides, and sigma phases are formed during aging at 500–1000 °C, giving rise to the increase in the hardness, while the incoherent sigma precipitate in the austenite matrix was detrimental to the toughness of alloys. In recent years, carbons have already been applied in HEAs gradually. Wu et al. [28] have reported that both the yield strength and the tensile strength of CoCrFeNiMnHEA were significantly increased by adding 0.5 at.% of C. N. Gao et al. [29] have studied the strengthening effect of NbC precipitation on the microstructure and property of FeCoCrNiMn HEA and found that 0.8 at.% of Nb/C addition can increase the yield strength and ultimate tensile strength to 732 MPa and 911 MPa, respectively, while maintaining a high elongation of 32%.

Many studies have shown that equal atomic ratios are not the necessary condition for the formation of single-phase solid solutions. For example, Tasan et al. [30] have investigated the effect of non-equal atomic ratios on the phase stability, deformation mechanism, and mechanical properties of FeCoCrNiMn HEA, and they found that the $Fe_{40}Mn_{27}Ni_{26}Co_5Cr_2$ alloy is composed of a stable single FCC structure, and the quaternary unequal atomic ratio $Fe_{37}Mn_{45}Co_9Cr_9$ alloy is also comprised of a single FCC equiaxed crystal structure after homogenization treatment. Ma et al. [31] have found that the $Fe_{42}Cr_{20}Ni_{30}Co_6Cr_2$ MEA contains only a single FCC phase. Stepanov et al. [32] have studied a series of quaternary Cr–Fe–Ni–Mn non-equal atomic ratio alloys, and they found that the $Fe_{40}Mn_{28}Ni_{28}Cr_4$, $Fe_{40}Mn_{28}Ni_{20}Cr_{12}$, and $Fe_{40}Mn_{28}Ni_{14}Cr_{18}$ alloys are all composed of a simple FCC structure.

Carbides are an effective hardening particle for improving the strength of the steels. For example, Scott et al. [33] have enhanced the strength of high manganese austenitic TWIP steels by TiC, NbC, and VC. Wang et al. [34] found that the ultrafine M_3C, M_7C_3, and $M_{23}C_6$ carbides are responsible for the enhanced strength of high chromium steels. VC and Mo_2C are hard phases with simple crystal structures, which are commonly formed in V-Mo-containing steels. VC/Mo_2C carbides usually show two main types of size distribution: one is the primary carbides with a size range of 1–10 μm formed during solidification, and the other is the fine strengthening secondary precipitates with a nanometer size generated from a supersaturated matrix during the aging treatment or when the steels are serviced at high temperature. The substantial strengthening effect of VC/Mo_2C carbides has been reported for various steel grades [35,36]. So far, few have rarely reported on the precipitation behavior of Mo_2C, VC, Cr_7C_3, etc., in FeCoCrNiHEAs, although these particles can be used to strengthen the alloy by second phase strengthening. Therefore, the purpose of this work is to use the hard Mo_2C and VC carbides to strengthen FCC-structured HEA using a high content of carbide-forming elements. There are two considerations that need to be taken into account when designing the alloy composition. Firstly, increasing the Fe content to above 50% on the basis of FeCoCrNi HEA can effectively reduce the cost of HEAs while still obtaining adequate entropy configuration to stabilize FCC solid solution over intermetallic compounds. Secondly, strong carbide-forming elements Mo and V and sufficient C element are added for promoting the precipitates of carbides. The investigated alloy is named as non-equal-atomic $Fe_{55}(CoCrNi)_{10}(MoV)_5C_5$, which can be classified as a medium-entropy alloy (MEA), according to the generally accepted definition that specifies MEA as an alloy with the configuration entropy between R and 1.5R, in which R is the gas constant. In this study, the influence of aging treatment on the microstructure evolution, precipitation behavior, and changes in the mechanical

properties of MEA was investigated and discussed. The results of this study can provide an easy approach to strengthen MEAs by tailoring their composition and aging treatment.

2. Experimental Procedures

$Fe_{55}(CoCrNi)_{10}(MoV)_5C_5$ MEA was prepared by the vacuum arc melting mixture of pure metals Fe, Co, Cr, Ni, Mo, V, (purity > 99.9%) and Fe-5 wt %C master alloys. The nominal and real compositions of the investigated alloy are shown in Table 1. Before alloy melting, the chamber was evacuated to ~5×10^{-2} Pa, followed by flushing twice using pure Ar. The ingot was flipped and remelted five times to ensure chemical homogeneity and finally cast into a cylindrical ingot with a size of Φ60 mm × 150 mm. Then, the alloy was aged at 400–1000 °C for 4 h followed by water quenching.

Table 1. Chemical compositions of $Fe_{55}(CoCrNi)_{10}(MoV)_5C_5$ medium-entropy alloy (MEA).

Elements (at %)	Fe	Co	Cr	Ni	Mo	V	C
Nominal composition	55	10	10	10	5	5	5
Real composition	49.56	12.05	11.02	11.56	5.35	5.69	5.1

The metallographic samples were prepared by mechanical grinding and then electropolished using a mixed solution of 20 vol.% perchloric acid, 10 vol.% glycerin, and 70 vol.% alcohol. The phase structure of the alloy was characterized using an X-ray diffractometer (Bruker D8-Advance, Germany) with a scanning speed of 2°/min and a 2θ range of 20–100°. According to Bragg's law ($n\lambda = 2d_{hkl}sin\theta$), the interplanar spacing (d_{hkl}) of the FCC matrix was obtained from its diffraction angles (θ), and the lattice parameter (a) of the FCC phase can be calculated using the following equation: $d_{hkl} = a/\left(h^2 + k^2 + l^2\right)^{1/2}$.

The field-emission scanning electron microscope (SEM, Zeiss Sigma, Oberkochen, Germany) was used to observe the microstructure of the alloy. TEM investigations were performed utilizing an FEI TecnaiG2 F20 microscope equipped with energy-dispersive spectrometer (EDS) (FEI, Hillsboro, OR, USA) at an accelerating voltage of 200 KV. The TEM sample was mechanically ground to a thickness of approximately 50 μm, which was followed by thinned using ion beam milling. The Image-pro-plus 6.0 software (Version 6.0.0.260, Media Cybernetics, Rockville, MD, USA) was applied to count the size of grains, the particle size, and the volume fractions of the precipitates.

A 200HVS-5 Vickers hardness tester was used to measure the hardness of the bulk alloy, and the test was carried out at a load of 1 kg and a holding time of 15 s. In order to ensure the accuracy of the data, 7 measurements were performed for determining the average value. The room temperature tensile tests were conducted on a UTS5105 electronic universal testing machine (SANS, Shenzhen, China) with a strain rate of 10^{-3}/s using dog-bone-shaped samples with a gauge length of 10 mm, width of 3 mm, and thickness of 1 mm. Three samples were tested for each state to ensure repeatability.

3. Results and Discussion

3.1. Age-Hardening Curve

The hardness curve of the investigated MEA after aging at 400–1000 °C for 4 h is shown in Figure 1. It can be seen that the hardness of the alloy increases at first and then decreases as the temperature increases. The hardness peak appears at 800 °C and increases from 253 HV in cast condition (not list in here in) to 326 HV (increased by 29%). When the temperature exceeds 800 °C, the hardness decreases gradually and reaches 289 HV at 1000 °C, indicating that the hardness still maintained a relatively high value compared to the hardness of the as-cast alloy even at a very high temperature.

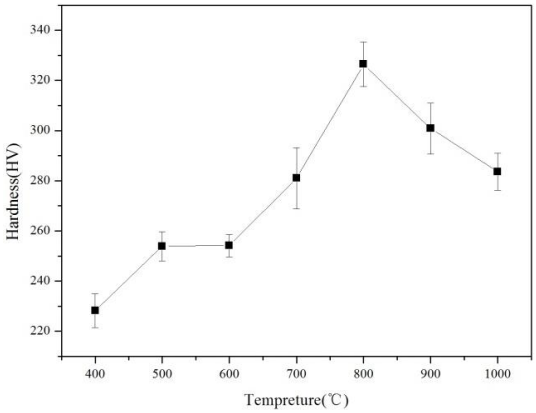

Figure 1. Hardness curve of the 4 h-aged alloys as a function of temperature.

3.2. Phase Analysis

Figure 2 shows the XRD patterns of the studied alloys in the as-cast condition and aged at 600–1000 °C for 4 h. It can be seen that the phase constitute of the as-cast alloy consisted of FCC, MC, and M_2C carbide. No other phases were found in the alloy after aging at 600–1000 °C within the limitation of the XRD detector. However, it can be noted that the 2θ for the 800 °C aged alloy apparently has shifted to the higher angle compared to those of the others. This indicates that the lattice constant of the FCC matrix has decreased significantly during aging at 800 °C, and it may be attributed to the abundant atoms precipitating from the matrix. The calculated lattice constant of the FCC matrix in different states shown in Figure 3 could verify this phenomenon. Contrary to the hardness curve, the lattice constant of the FCC decreases first and then increases as the aging temperature rises. The lattice constant of the FCC matrix in the cast alloy was 0.35994 nm, and it decreased to the lowest value of 0.35927 nm when the temperature increases to 800 °C. As the aging temperature exceeds 800 °C, the lattice constant begins to increase, indicating that the precipitated phase has re-dissolved into the FCC matrix and increased the lattice constant of the matrix.

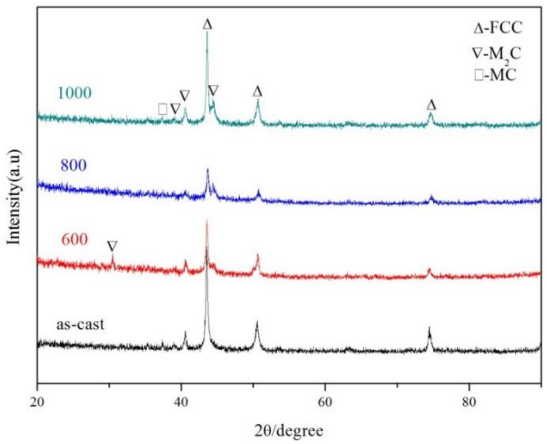

Figure 2. XRD patterns of the as-cast and 4 h-aged alloys.

The phase constitute of the investigated alloy can be predicted by means of the phase criterion of HEAs (only consider metallic elements) proposed by Y. Zhang [7]; this criterion and related parameters contain ΔS_{mix} (the mixing entropy), ΔH_{mix} (the mixing enthalpy), $\Delta\chi$ (the Pauling electronegativity difference), δ (the atomic-size difference), VEC (the valence electron concentration), and Ω (ratio of entropy to enthalpy). The terms δ and $\Delta\chi$ are the standard deviation of atomic sizes and electronegativity in the alloy, respectively, reflecting the discrete degree of distribution of atom size and electronegativity in an alloy. The calculated methods for these parameters are conducted according to the thermodynamic and Hume-Rothery rules for the formation of solid solution, and the results are shown in Table 2. It can be

found that the investigated alloy satisfies the conditions of $\delta < 6.6\%$, -22 KJ/mol $< \Delta H_{mix} < 5$ KJ/mol , $\Omega \geq 1.1$, $\Delta\chi \leq 0.175$, $VEC > 6.87$ for the formation of a stable FCC solid solution. However, in the present study, the results of XRD analyses showed that FCC phase and carbide were the phase components of the as-cast alloy. Based on the thermodynamic concept, a system attempt to minimize its Gibbs free energy (ΔG_{mix}) in order to achieve a stable equilibrium state, in which ΔG_{mix} is known to be related to the mixing enthalpy (ΔH_{mix}) and mixing entropy (ΔS_{mix}), and the relation among these three parameters can be expressed as shown in Equation (1) [37].

$$\Delta G_{mix} = \Delta H_{mix} - T\Delta S_{mix} \quad (1)$$

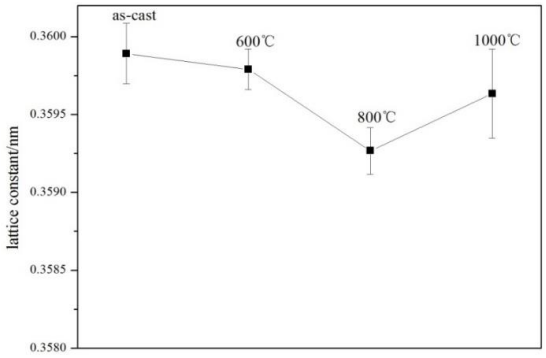

Figure 3. The calculated lattice constant of the face-centered cubic (FCC) matrix of the as-cast and 4 h-aged alloys.

Table 2. Calculated parameters of ΔS_{mix} , ΔH_{mix}, $\Delta\chi$, δ, VEC, and Ω for investigated MEA.

Alloy	ΔS_{mix} (J/mol·k)	ΔH_{mix} (KJ/mol)	$\Delta\chi$	δ/%	VEC	Ω
$Fe_{55}(CoCrNi)_{10}(MoV)_5C_5$	10.967	−3.23	0.14	5.9	7.45	6.15

The values of the mixing enthalpy of binary systems ($\Delta H_{mix}AB$) for the investigated alloy are listed in Table 3. As can be shown, the C–V, C–Mo binary systems have the most negative mixing of enthalpy (−82 KJ/mol, −67 KJ/mol, respectively), which means that the vanadium carbide and molybdenum carbide could be the phases with high thermodynamic stability. Therefore, for the investigated alloy, the addition of C results in the formation of MC and M_2C carbides rather than dissolving into the matrix to form solid solution. So, there are also carbides in the alloy except for the FCC phase.

Table 3. The values of the mixing enthalpy of binary systems ($\Delta H_{mix}AB$) [38]/ KJ·mol^{-1}.

Element	C	V	Cr	Fe	Co	Ni	Mo
C	-	−82	−61	−50	−42	−39	−67
V		-	−2	−7	−14	−18	0
Cr			-	−1	−4	−7	0
Fe				-	−1	−2	−2
Co					-	0	−5
Ni						-	−7
Mo							-

3.3. Microstructures

Figure 4 shows the microstructure of the investigated alloy in different conditions. As shown in Figure 4a, the microstructure of the as-cast alloy was characterized by a typical dendrite structure with an average grain size of about 53 μm (For the grain size, using Image-pro-plus 6.0 software for statistics, select at least 20 grains for statistics, repeat three times to get the average value.) and many

coarse carbides distributed in the interdendrite. Combined with the results of XRD, the dendrite structure can be identified as FCC phase, and bright white layered carbide and gray chrysanthemum carbide were M_2C and MC, respectively. Figure 4b shows the microstructure of the alloy after aging at 600 °C; no obvious changes of carbide in shape and distribution were found compared with those of the as-cast alloy. After aging at 800 °C, it can be seen from Figure 4c that there are many particles inside the grains. A detailed examination indicates that these particles are cubical or needle-shaped precipitates, and the needles appears as a list of discontinuously distributed precipitates and tend to be spread around coarser cubical particles (marked by red circle in Figure 4d). When the temperature increases to 1000 °C, it can be found that the particles inside the grains began to grow in size and shape from fine cubical into granular or coarse rod-like particles (Figure 4e,f).

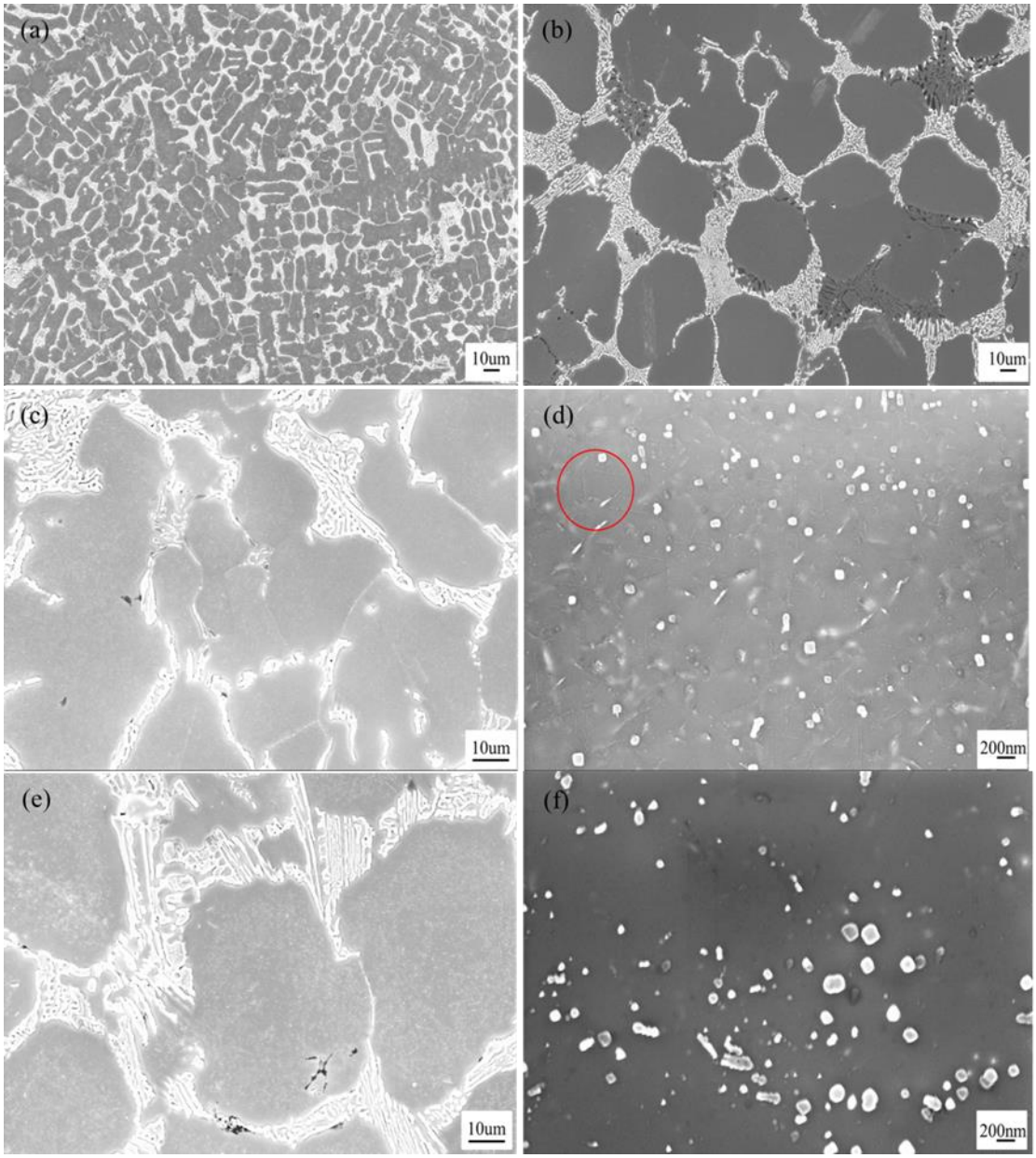

Figure 4. Microstructure of as-cast alloy and aging at different temperatures: (**a**) as-cast; (**b**) 600 °C/4 h aged; (**c**) 800 °C/4 h aged, (**d**) the high magnification imaging of (**c**); (**e**) 1000 °C/4 h aged; (**f**) the high magnification imaging of (**e**).

The particle size distribution and volume fraction of alloys after aging at 800 °C and 1000 °C are presented in Figure 5. The average diameter and volume fraction of precipitates in the 800 °C aged alloy were measured to be about 46 nm, 5.6%, respectively. After aging at 1000 °C, the average diameter of precipitates increased to 86 nm, while the volume fraction decreased to 4.7%.

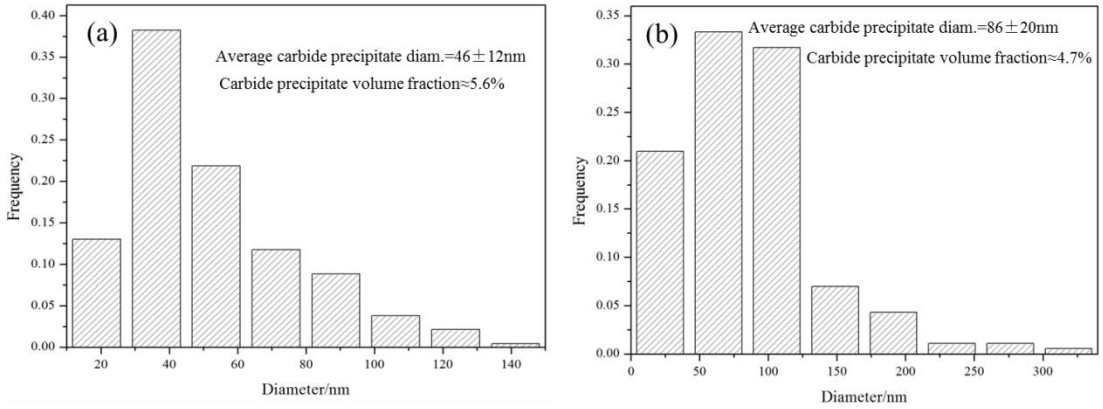

Figure 5. Diameter distribution and volume fraction of precipitates in the 800 °C/4 h (**a**) and 1000 °C/4 h (**b**) aged alloys.

Figure 6a shows the TEM images of the granular particles in the alloy after aging at 800 °C for 4 h. The particle was identified by electron diffraction as VC carbide with a FCC structure, and the EDS analysis of this particle presented in Figure 6b shows unambiguously that it was enriched with a V element. VC carbide is a hard and brittle phase, and the densely distributed VC that exists in the matrix of 800 °C aged alloy can play an important role for pinning dislocations, leading to the highest hardness. The typical morphology of the fine needle-like precipitates is shown in Figure 7. It can be found that the needles were composed of many discontinuously distributed fine particles with sizes of approximately 29 nm (Figure 7a,b), which is consistent with the observation in Figure 4c. These needles were usually observed to be distributed along the larger particles (marked by arrows 1, 2 in Figure 7c). This is probably because the areas near coarse particles have a lot of dislocations and carbon atoms easily segregate on these locations during the aging process. Figure 8a shows the morphology of fine VC carbides distributed along dislocation lines, and the result of EDS (obtained from area marked by arrow in Figure 8b) further confirms that these particles mainly contain a V element. It is noted that the high content of Fe may originate from the matrix due to the size of the particle being smaller than the size of the electron beam spot. Figure 8c illustrates the HRTEM image of the fine precipitates, and the result shows that the particle is spherical with a size of 8–10 nm (marked by a red rectangle), and the corresponding Fast Fourier Transformation (FFT) shown in Figure 8d confirms that this particle is VC having a cubic-on-cubic crystallographic relationship with the FCC matrix, which is consistent with the results in some traditional iron base alloys [25]. Through the above analysis, it can be inferred that it is the large amount of precipitation of these nano-scaled VC carbides playing a significant role in precipitation strengthening and dispersion strengthening, leading to the hardness peak in the alloy after aging at 800 °C for 4 h. As the temperature increased, the particles gradually grow up, and the effect of precipitation strengthening decreased, resulting in a decrease in the hardness value.

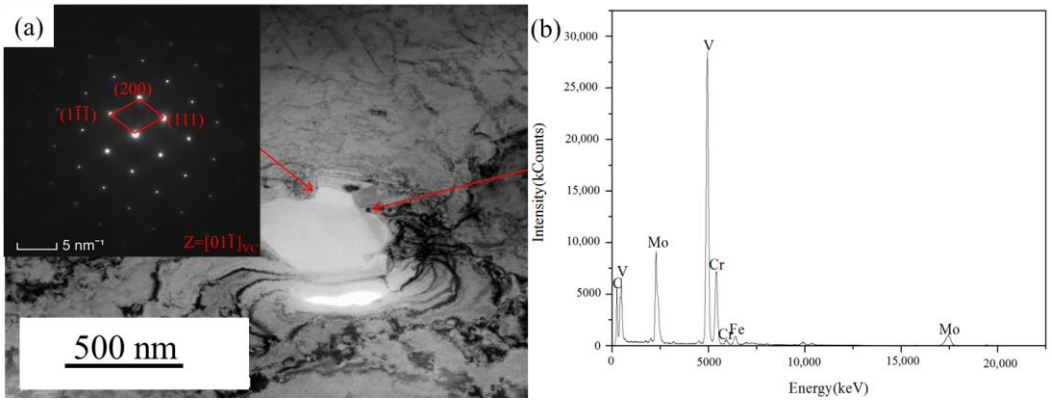

Figure 6. TEM images (**a**) and energy-dispersive spectrometer (EDS) analysis (**b**) of granular particles in the alloy after aging at 800 °C for 4 h. The inset in (**a**) is the corresponding selected diffraction from the particle.

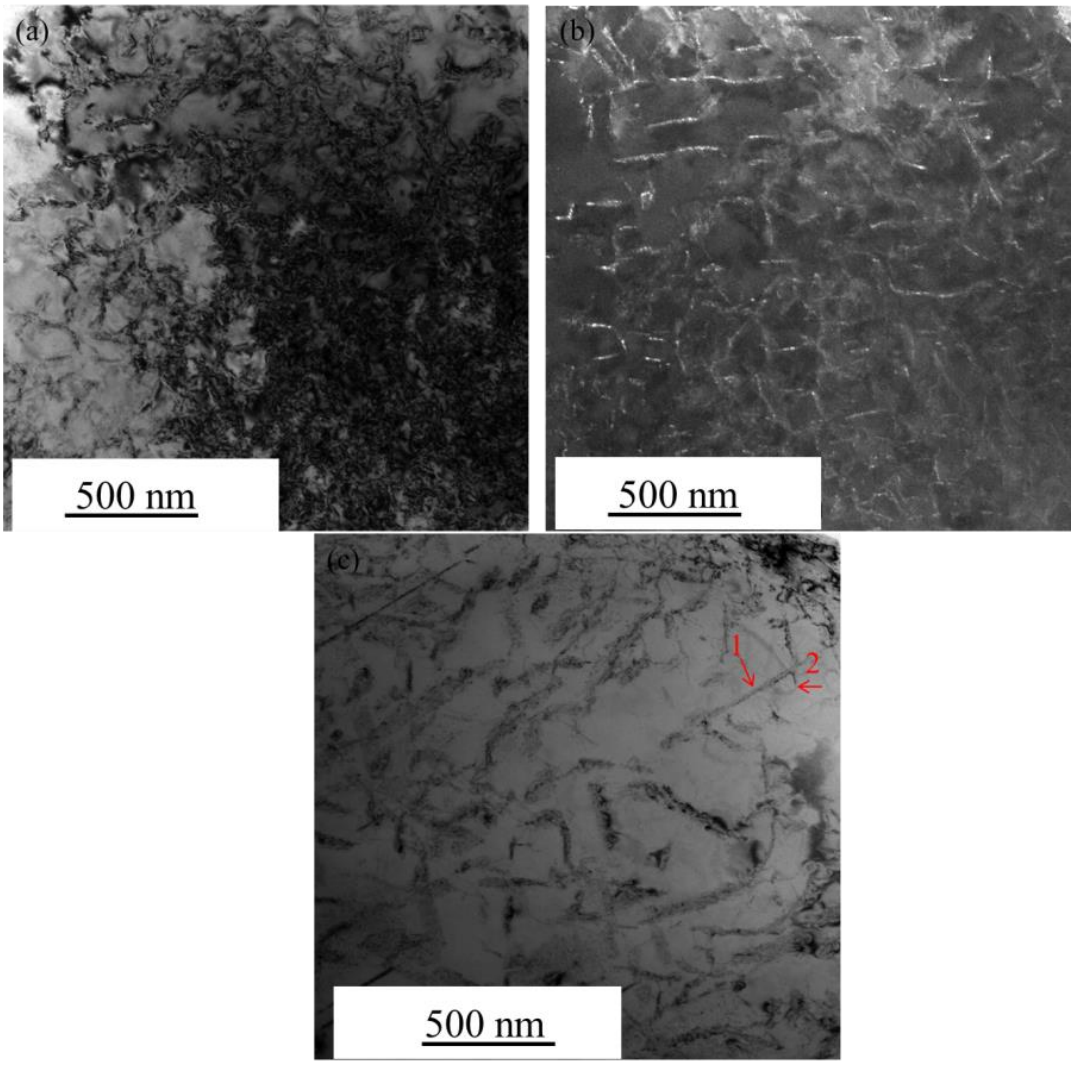

Figure 7. Typical morphology and distribution of particles in alloy after aging at 800 °C for 4 h: (**a**) bright field; (**b**) dark field of rod-like VCparticles; (**c**) VC particles distributed along dislocation lines.

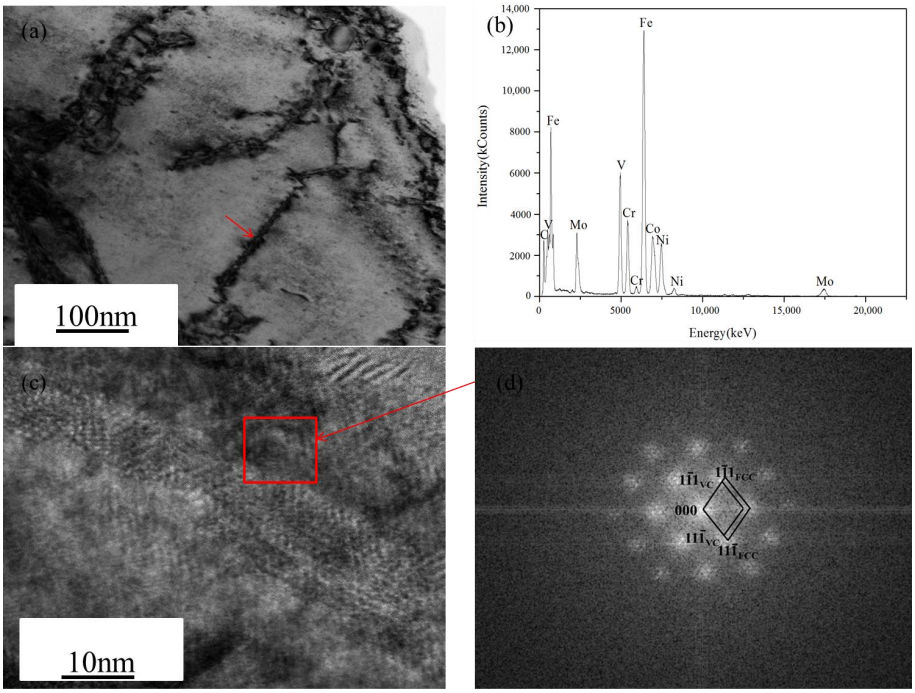

Figure 8. TEM micrograph of nano-sized VC carbides in alloy after aging at 800 °C for 4 h: (**a**) fine VC carbides precipitating along dislocation lines, (**b**) the EDS analysis of fine VC carbides marked by arrow in (**a**); (**c**) HRTEM image of fine VC precipitates; (**d**) Fast Fourier Transformation (FFT) image of precipitates marked by red rectangle in (**c**).

3.4. Tensile Properties

Figure 9 shows the engineering stress-strain curves of the alloys in different states. It can be seen that the tensile strength and elongation of the as-cast alloy was low. When the alloy was aged, both the ductility and strength increased. The mechanical properties of the alloys in different states are collected in Table 4. As can be shown, the tensile strength of the alloy reached a maximum value of 626 MPa after aging at 800 °C for 4 h, which increased by 94% compared to those of the as-cast alloy, while the elongation increased from 1.2% to 6.2%. As the temperature increases to 1000 °C, its tensile strength decreased to 548 MPa, and the elongation decreased to 2.9%. Figure 10 shows the tensile fracture morphology of the alloys at different states. As shown in Figure 10a,b, the fracture surface of the as-cast alloy is characterized by cleavage facets, secondary cracks, and a small amount of tearing ridges, suggesting that it belongs to brittle fracture. This is because there are a large number of network carbides on the grain boundary, which can seriously reduce the plasticity of the alloy. Figure 10c,d show the fracture morphology of the alloy after aging at 800 °C for 4 h, and it can be found that there are more tearing edges and increased dimples except for some river-like cleavage facets, indicating that the fracture mechanism belongs to quasi-cleavage fracture. The improvement of ductility for the 800 °C aged alloy might be attributed to the large number of carbide particles dispersed throughout the matrix effectively released local stress concentration during deformation, thus making the cracks difficult to initiate and propagate. On the other hand, the precipitation of the secondary phase particles can promote the nucleation of microscopic voids and the occurrence of local plastic deformation, thus increasing elongation [39]. The fracture morphology of the 1000 °C aged alloy shown in Figure 10e,f manifests a complex fracture surface of river-like cleavage facets, cleavage steps, and a few dimples, indicating that the type of fracture belongs to brittle fracture. As depicted above, the fine precipitates have coarsening and aggregating after being aged at 1000 °C. Some studies have pointed out that the larger carbides can weaken the effect of the precipitation strengthening, leading to the decrease in strength [40,41]. As the VC carbides grow up, a stress concentration is

generated around them during the deformation process, and the crack is easy to form and expand, thus reducing the ductility.

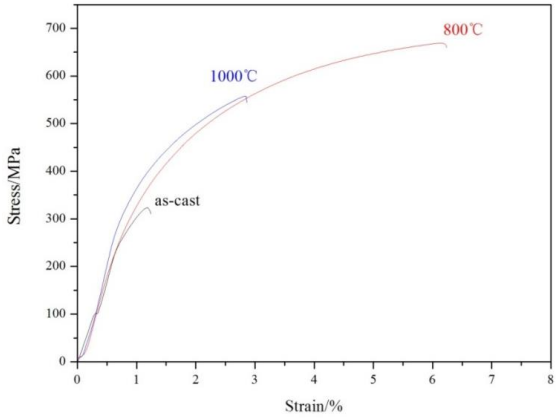

Figure 9. Engineering stress-strain curves of the alloys in different states.

Table 4. Yield strength, ultimate tensile strength, and elongation of alloys in different states.

States	Yield Strength σ_s/MPa	Ultimate Tensile Strength σ_b/MPa	Elongation ε/%
As-cast	313	322	1.2
800 °C	349	626	6.2
1000 °C	374	548	2.9

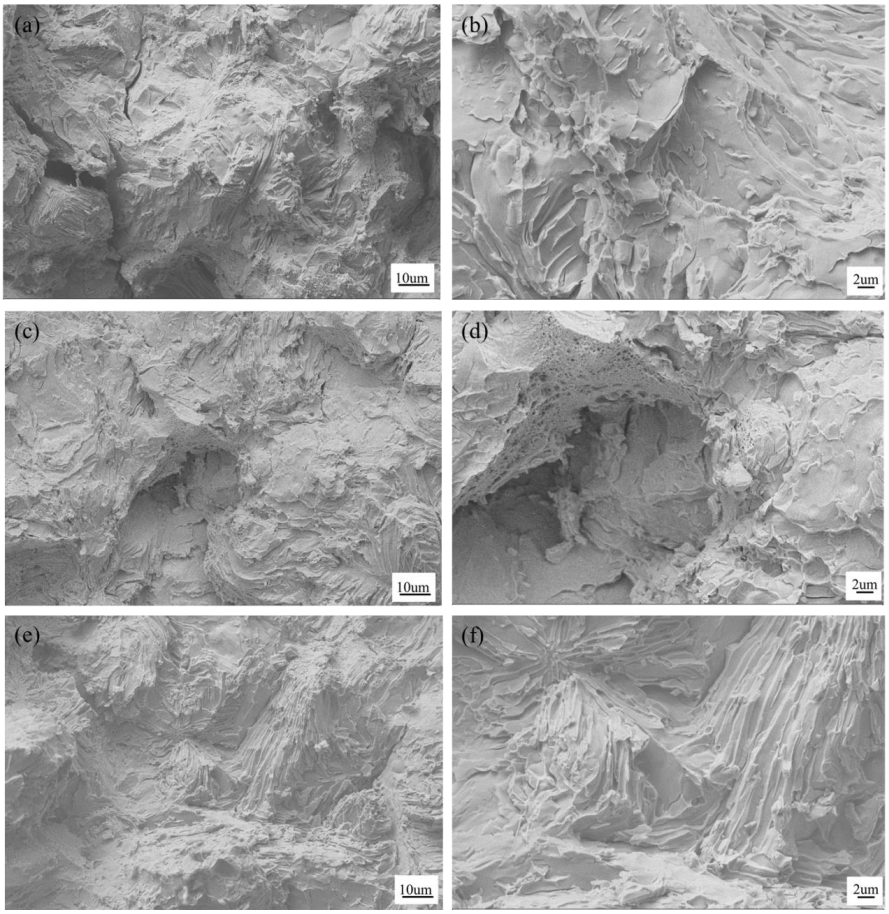

Figure 10. The fracture morphologies of the investigated alloys: (**a**,**b**) as-cast; (**c**,**d**) 800 °C aged for 4 h; (**e**,**f**) 1000 °C aged for 4 h.

4. Conclusions

The effect of aging temperatures on the microstructure evolution, carbide precipitation behavior, and properties of the $Fe_{55}(CoCrNi)_{10}(MoV)_5C_5$ MEA were investigated, and the following conclusions can be drawn as follows:

(1) The microstructure of the as-cast alloy is composed of a FCC dentritic structure, interdentritic M_2C, and MC carbide. The average grain size of the investigated alloy was approximately 53 μm. The very low negative mixing enthalpy of C–V and C–Mo binary systems makes carbon tend to combine with Mo and V to form carbides rather than forming a solid solution.

(2) Aging hardening is present over the temperature range of 600–1000 °C. The hardness peak appears at 800 °C, which raises the hardness increases from 253 HV in as-cast to 326 HV, due to a plethora of nano-scale VC carbides precipitating from the matrix. As the aging temperature rises, the VC particle size increases and the volume fraction decreases, thus decreasing the hardening effect.

(3) 800 °C/4 h aged alloy has the highest ultimate tensile strength of 626 MPa and a relatively good elongation. The uniformly distributed nano-sized VC precipitates throughout the FCC matrix contributed to the high strength and reasonable ductility of the MEA.

Author Contributions: Conceptualization, H.W. and L.H.; methodology, P.O.; software, Y.W.; validation, H.W., L.H. and H.Z.; formal analysis, D.H.; investigation, D.H.; resources, L.H.; data curation, D.H.; writing—original draft preparation, D.H.; writing—review and editing, H.W.; visualization, H.W.; supervision, H.Z.; project administration, H.W.; funding acquisition, H.Z. All authors have read and agreed to the published version of the manuscript.

Funding: This research was funded by Open Foundation of State Key Laboratory for Advanced Metals and Materials, University of Science and Technology Beijin (grant number 2018-Z01), the Scientific Research Project Fund of Jiangxi Provincial Education Department (grant number GJJ180479), Natural Science Foundation of Jiangxi Province (grant number 20202BABL204010) and Program of the University Students' Innovation and Pioneering (grant number DC2019-034). andthe APC was funded by Open Foundation of State Key Laboratory for Advanced Metals and Materials.

Conflicts of Interest: The authors declare no conflict of interest.

References

1. Yeh, J.W.; Chen, S.K.; Lin, S.J.; Gan, J.Y.; Chin, T.S.; Shun, T.T.; Tsau, C.H.; Chang, S.Y. Nanostructured high-entropy alloys with multiple principal elements: Novel alloy design concepts and outcomes. *Adv. Eng. Mater.* **2004**, *6*, 299–303. [CrossRef]
2. Miracle, D.B.; Senkov, O.N. A critical review of high entropy alloys and related concepts. *Acta Mater.* **2017**, *122*, 448–511. [CrossRef]
3. Ye, Y.F.; Wang, Q.; Lu, J.; Liu, C.T.; Yang, Y. High-entropy alloy: Challenges and prospects. *Mater. Today* **2016**, *19*, 349–362. [CrossRef]
4. Zhang, Y.; Zuo, T.T.; Tang, Z.; Gao, M.C.; Dahmen, K.A.; Liaw, P.K.; Lu, Z.P. Microstructures and properties of high-entropy alloys. *Prog. Mater. Sci.* **2014**, *61*, 1–93. [CrossRef]
5. He, F.; Wang, Z.; Wu, Q.; Niu, S.; Li, J.; Wang, J.; Liu, C.T. Solid solution is land of the Co-Cr-Fe-Ni high entropy alloy system. *Scr. Mater.* **2017**, *131*, 42–46. [CrossRef]
6. Zhang, W.R.; Liaw, P.K.; Zhang, Y. Science and technology in high-entropy alloys. *Sci. China Mater.* **2018**, *61*, 2–22. [CrossRef]
7. Wang, W.R.; Wang, W.L.; Wang, S.C.; Tsai, Y.C.; Lai, C.H.; Yeh, J.W. Effects of Al addition on the microstructure and mechanical property of $Al_xCoCrFeNi$ high-entropy alloys. *Intermetallics* **2012**, *26*, 44–51. [CrossRef]
8. Li, Z.; Pradeep, K.G.; Deng, Y.; Raabe, D.; Tasan, C.C. Metastable high-entropy dual-phase alloys overcome the strength-ductility trade-off. *Nature* **2016**, *534*, 227–230. [CrossRef]
9. Stepanov, N.D.; Shaysultanov, D.G.; Chernichenko, R.S.; Yurchenko, N.Y.; Zherebtsov, S.V.; Tikhonovsky, M.A.; Salishchev, G.A. Effect of thermomechanical processing on microstructure and mechanical properties of the carbon-containing CoCrFeNiMn high entropy alloy. *J. Alloys Compd.* **2017**, *693*, 394–405. [CrossRef]
10. Qiu, X.W.; Wu, M.J.; Liu, C.G.; Zhang, Y.P.; Huang, C.X. Corrosion performance of $Al_2CrFeCo_xCuNiTi$ high-entropy alloy coatings in acid liquids. *J. Alloys Compd.* **2017**, *708*, 353–357. [CrossRef]

11. Seol, J.B.; Bae, J.W.; Li, Z.; Han, J.C.; Kim, J.G.; Raabe, D.; Kim, H.S. Boron doped ultrastrong and ductile high-entropy alloys. *Acta Mater.* **2018**, *151*, 366–376. [CrossRef]
12. Riva, S.; Tudball, A.; Mehraban, S.; Lavery, N.P.; Brown, S.G.R.; Yusenko, K.V. A novel High-Entropy Alloy-based composite material. *J. Alloys Compd.* **2018**, *730*, 544–551. [CrossRef]
13. Lin, C.M.; Tsai, H.L.; Bor, H.Y. Effect of aging treatment on microstructure and properties of high-entropy $Cu_{0.5}$CoCrFeNi alloy. *Intermetallics* **2010**, *18*, 1244–1250. [CrossRef]
14. Ren, B.; Liu, Z.X.; Li, D.M.; Shi, L.; Cai, B.; Wang, M.X. Corrigendum to "Effect of elemental interaction on microstructure of CuCrFeNiMn high-entropy alloy system". *J. Alloys Compd.* **2010**, *503*, 538. [CrossRef]
15. Tsai, K.Y.; Tsai, M.H.; Yeh, J.W. Sluggish diffusion in Co–Cr–Fe–Mn–Ni high-entropy alloys. *Acta Mater.* **2013**, *61*, 4887–4897. [CrossRef]
16. Chuang, M.H.; Tsai, M.H.; Wang, W.R.; Lin, S.J.; Yeh, J.W. Microstructure and wear behavior of $Al_xCo_{1.5}CrFeNi_{1.5}Ti_y$ high-entropy alloys. *Acta Mater.* **2011**, *59*, 6308–6317. [CrossRef]
17. Li, X.F.; Feng, Y.H.; Liu, B.; Yi, D.H.; Yang, X.H.; Zhang, W.D.; Chen, G.; Liu, Y.; Bai, P.K. Influence of NbC particles on microstructure and mechanical properties of AlCoCrFeNi high-entropy alloy coatings prepared by laser cladding. *J. Alloys Compd.* **2019**, *788*, 485–494. [CrossRef]
18. Jiang, H.; Han, K.M.; Qiao, D.X.; Lu, Y.P.; Chao, Z.Q.; Li, T.J. Effects of Ta Addition on the Microstructures and Mechanical Properties of CoCrFeNi High Entropy Alloy. *Mater. Chem. Phys.* **2018**, *210*, 43–48. [CrossRef]
19. Shun, T.T.; Chang, L.Y.; Shiu, M.H. Age-hardening of the $CoCrFeNiMo_{0.85}$ high-entropy alloy. *Mater. Charact.* **2013**, *81*, 92–96. [CrossRef]
20. He, F.; Wang, Z.J.; Liu, S.Z.; Wu, Q.F.; Li, J.J.; Wang, J.C.; Liu, C.T.; Dang, Y.Y. Strengthening the $CoCrFeNiNb_{0.25}$ high entropy alloy by FCC precipitate. *J. Alloys Compd.* **2016**, *667*, 53–57. [CrossRef]
21. Saenarjhan, N.; Kang, J.H.; Kim, S.J. Effects of carbon and nitrogen on austenite stability and tensile deformation behavior of 15Cr-15Mn-4Ni based austenitic stainless steels. *Mater. Sci. Eng. A* **2019**, *742*, 608–616. [CrossRef]
22. Conrad, H. Effect of interstitial solutes on the strength and ductility of titanium. *Prog. Mater. Sci.* **1981**, *26*, 123–403. [CrossRef]
23. Urrutia, I.G.; Raabe, D. Multistage strain hardening through dislocation substructure and twinning in a high strength and ductile weight-reduced Fe-Mn-Al-C steel. *Acta Mater.* **2012**, *60*, 5791–5802. [CrossRef]
24. Gutierrez, I.; Raabe, D. Microbanding mechanism in a Fe-Mn-C high-Mn twinning-induced plasticity steel. *Scr. Mater.* **2013**, *69*, 53–56. [CrossRef]
25. Ou, P.; Xing, H.; Sun, J. Precipitation of nanosized MX at coherent Cu-rich phases in Super304H austenitic steel. *Metall. Mater. Trans. A* **2015**, *46*, 1–5. [CrossRef]
26. Ou, P.; Li, L.; Xie, X.F.; Sun, J. Steady-state creep behavior of Super304H austenitic steel at elevated temperatures. *Acta Metall. Sin.* (*Engl. Lett.*) **2015**, *28*, 1336–1343. [CrossRef]
27. Anburaj, J.; Nazirudeen, S.S.M.; Narayanan, R.; Anandavel, B.; Chandrasekar, A. Ageing of forged superaustenitic stainless steel: Precipitate phases and mechanical properties. *Mater. Sci. Eng. A* **2012**, *535*, 99–107. [CrossRef]
28. Wu, Z.; Parish, C.M.; Bei, H. Nano-twin mediated plasticity in carbon-containing FeNiCoCrMn high entropy alloys. *J. Alloys Compd.* **2015**, *647*, 815–822. [CrossRef]
29. Gao, N.; Lu, D.H.; Zhao, Y.Y.; Liu, X.W.; Liu, G.H.; Wu, Y.; Liu, G.; Fan, Z.T.; Lu, Z.P.; George, E.P. Strengthening of a CrMnFeCoNi high-entropy alloy by carbide precipitation. *J. Alloys Compd.* **2019**, *792*, 1028–1035. [CrossRef]
30. Tasan, C.C.; Deng, Y.; Pradeep, K.G.; Yao, M.J.; Springer, H.; Raabe, D. Composition Dependence of Phase Stability, Deformation Mechanisms, and Mechanical Properties of the CoCrFeMnNi High-Entropy Alloy System. *JOM* **2014**, *66*, 1993–2001. [CrossRef]
31. Ma, D.C.; Yao, M.J.; Pradeep, K.G.; Tasan, C.C.; Springer, H.; Raabe, D. Phase stability of non-equiatomic CoCrFeMnNi high entropy alloys. *Acta Mater.* **2015**, *98*, 288–296. [CrossRef]
32. Stepanov, N.D.; Shaysultanov, D.G.; Tikhonovsky, M.A.; Salishchev, G.A. Tensile properties of the Cr-Fe-Ni-Mn non-equiatomic multicomponent alloys with different Cr contents. *Mater. Des.* **2015**, *87*, 60–65. [CrossRef]
33. Scott, C.; Remy, B.; Collet, J.L.; Cael, A.; Bao, C.; Danoix, F.; Malard, B.; Curfs, C. Precipitation strengthening in high manganese austenitic TWIP steels. *Int. J. Mater. Res.* **2011**, *102*, 538–549. [CrossRef]

34. Wang, Y.; Li, M.Y.; Han, B.; Han, T.; Cheng, Y.Y. Influence of secondary carbides precipitation and transformation on the secondary hardening of laser melted high chromium steel. *J. Mater. Sci.* **2010**, *45*, 3442–3447. [CrossRef]
35. Xu, W.; Rivera-Diaz-del-Castillo, P.E.J.; Yan, W.; Yang, K.; Martin, D.S.; Kestens, L.A.I.; van der Zwaag, S. A new ultrahigh-strength stainless steel strengthened by various coexisting nanoprecipates. *Acta Mater.* **2010**, *58*, 4067–4075. [CrossRef]
36. Wang, H.B.; Hou, L.G.; Li, Y.B.; Ou, P.; Shen, L.; Wen, X.E.; Cui, H.; Zhang, J.S. Effect of niobium on the secondary precipitates and tempering resistance of spray-formed M3:2 high-speed steel. *J. Mater. Eng. Perform.* **2019**, *28*, 926–937. [CrossRef]
37. Shao, L.; Zhang, T.; Li, L.; Zhao, Y.H.; Huang, J.F.; Liaw, P.K.; Zhang, Y. A low-cost lightweight entropic alloy with high strength. *J. Mater. Eng. Perform.* **2018**, *27*, 6648–6656. [CrossRef]
38. Takeuchi, A.; Inoue, A. Classification of bulk metallic glasses by atomic size difference, heat of mixing and period of constituent elements and its application to characterization of the main alloying element. *Mater. Transm.* **2005**, *46*, 2817–2829. [CrossRef]
39. Zhong, Q.P.; Zhao, Z.H. *Fractography*; Higher Education Press: Beijing, China, 2006.
40. Kamikawa, N.; Abe, Y.; Miyamoto, G.; Funakawa, Y.; Furuhara, T. Erratum to "Tensile Behavior of Ti, Mo-added Low Carbon Steels with Interphase Precipitation". *ISIJ Int.* **2014**, *54*, 212–221. [CrossRef]
41. Hao, L.H.; Ji, X.; Zhang, G.Q.; Zhao, W.; Sun, M.Y.; Peng, Y. Carbide precipitation behavior and Mechanical properties of micro-alloyed medium Mn steel. *J. Mater. Sci. Technol.* **2020**, *47*, 122–130. [CrossRef]